SCIENTIFIC REPORTS
natureresearch

Check for updates

OPEN

Ab initio calculations of conduction band effective mass parameters of thermoelectric $Mg_2X_{1-x}Y_x$ (X, Y = Si, Ge, Sn) alloys

Juan M. Guerra✉, **Carsten Mahr**, **Marcel Giar**, **Michael Czerner** & **Christian Heiliger**

Since there are still research interests in the physical properties of quasi-binary thermoelectric $Mg_2X_{1-x}Y_x$ alloys, with X, Y = Si, Ge, Sn, we present an ab initio analysis that yields the relative formation energy and effective masses of the conduction bands, in the whole compositional range x. We base our calculations on the full-relativistic Korringa, Kohn and Rostocker (KKR) Green's functions formalism within the coherent potential approximation (CPA). Formation energies, measured relative to the end Mg_2X compounds, show no excess energy for the $Mg_2Si{-}Mg_2Ge$ substitution thus indicating a complete solubility. In contrast, concave and asymmetric formation energies for intermediate compositions in the $Mg_2X{-}Mg_2Sn$ alloys manifest a miscibility gap. With this basis, we compute and discuss the crossing of the conduction bands observed in *n*-type $Mg_2X_{1-x}Sn_x$ materials. We present direction- and band-dependent effective masses using a generalized single parabolic band effective mass approximation to discuss anisotropic effects, to interpret available experimental and theoretical data, and to predict intermediate and not yet published transport parameters on these alloys.

The physical and chemical properties of the *p*-type thermoelectric Mg_2X (X = Si, Ge, Sn) semiconductors, and their intermediate alloys, are still under an intense research activity since they represent a rich scenario for green-technological applications[1–11]. Among the isoelectronic X elements, Si is considerably the cheapest, and despite of the scarceness and relatively higher costs of production, Ge and Sn are regarded as the best substitutions for alloying[12,13]. The thermoelectric performance of Mg_2Si has shown to be substantially improved when Si is replaced by Sn due to an enrichment of its electronic density of states (DOS)—thus its power factor (PF)—and other induced detrimental effects on its phonons contribution to thermal transport[14].

A long standing theoretical and experimental record of research has been presented, mostly concentrated in Mg_2X crystals and $Mg_2Si_{1-x}Sn_x$ alloys, and their fundamental properties are not yet completely understood[15–20]. For instance, the volumetric mismatch between Mg_2Si (or Mg_2Ge) and Mg_2Sn has been shown to cause thermodynamical instability—the *miscibility gap*—and therefore to induce Mg_2X-rich phases, clusters, and inhomogeneities[21–23]. The complete solubility of $Mg_2Si_{1-x}Ge_x$ has been successfully demonstrated[15,24–27]. In the remaining $Mg_2X_{1-x}Sn_x$ systems, X = Si, Ge, the experiments on solid solutions have shown that solubility depends rather upon the preparation method and experimental conditions[23,28,29]. No complete and stable solubility has been demonstrated[1].

On the other hand, the improvement of the electronic properties has been associated to a degeneracy of the conduction bands controlled by the composition x in $Mg_2Si_{1-x}Sn_x$ and $Mg_2Ge_{1-x}Sn_x$, not present in $Mg_2Si_{1-x}Ge_x$[14]. All alloys have shown to improve their thermoelectric performance, but only $Mg_2Si_{1-x}Sn_x$ and $Mg_2Si_{1-x}Sn_x$ present a peak of performance at the composition where the conduction bands cross, i.e., at the *crossing point*[30]. There is no yet clear consensus about the exact composition x and temperature at which the crossing occur, and the effect of alloying on the electronic states and transport properties. Its importance lies in the fact that controlling and engineering the degeneracy of the conduction bands through alloying represents a promising venue to improve the electronic PF without doping[31].

Institut für Theoretische Physik, Justus-Liebig-Universität (University of Giessen), 35392 Giessen, Germany. ✉email: Juan-Manuel.Guerra@theo.physik.uni-giessen.de

Furthermore, there are still challenges in these systems, e.g., the search of the best dopants to design an efficient and environmentally friendly *n*-type sample—for the construction of a thermoelectric generator—and at the same time to suppress bipolar contributions to transport, etc.[32–36].

We use Green's functions based density functional theory (DFT)—ab initio—calculations to approach a description of the electronic properties of $Mg_2X_{1-x}Y_x$ alloys. To better understand the stability of these alloys and to improve the electronic DOS of these materials, we compute the relative formation energy and electronic bands effective masses using the coherent potential approximation (CPA) that describes perfectly random and homogeneous bulk alloys. We compare our calculations to available experimental and theoretical data and they show a very good agreement. This allows us to interpret and predict intermediate data not yet reported, specially in the case of $Mg_2Ge_{1-x}Sn_x$.

Results

Total energy calculations.

Minimization of the *ground state* DFT total energy, with respect to small variations of the unit cell volume, allows us to find the structure equilibrium. We have reported that, besides the usual and system dependent underestimations of the local density approximation (LDA) to the exchange and correlation potentials, the minimized lattice constant of $Mg_2X_{1-x}Y_x$ varies non-linearly with the alloy composition x, therefore deviating from the empirical Vegard's law[37]. This non-linearity is even more remarkable when the mismatch between the atomic masses of the substituted X and Y elements increases, i.e., for X = Si, Ge and Y = Sn[38]. This non-linearity is also reflected in the fundamental energy gaps and effective masses of the valence bands.

Total energy calculations have also been powerful to predict mechanical properties such as the bulk modulus and its derivative through a Murnaghan–Birch equation of state[39]. DFT total energy is the main ingredient to define the compounds' formation energy to study and predict their stability through the construction of phase diagrams[40]. Under the DFT physical conditions, at $T = 0$ K and $P = 0$ Pa, where the entropy contributions are negligible, the formation energy of a compound or alloy—its enthalpy of formation—permits to find the stable phases in the chemical space of compositions (x) through the so called convex hull, defined by the stable phases of the compounds. In turn, DFT formation energies have been widely useful to predict stable and meta-stable structures at using high-throughput computing and machine learning techniques[41,42]. Nonetheless, in order to study stability at room or higher temperatures, extra contributions coming from the entropy of phonons are present and possible phase transition may occur[43].

Therefore, we take the DFT total energy to construct the relative formation energy diagram of $Mg_2X_{1-x}Y_x$ by assuming stable phases of the end compounds, i.e., at $x = 0$ and $x = 1$. Hence, positive (negative) relative formation energies mean that at zero temperature the compound is less (more) likely to exist compared to Mg_2X[44].

We consider the on-site substitution between the X-elements at the edge of the unit cell, since this substitution (X_Y) is energetical and thermodynamically more likely to be present compared to the substitution Mg_Y[32,45–48]. We take the DFT total energy E and define the formation energy of Mg_2X, obtained through the reaction

$$2\mathrm{Mg} + \mathrm{X} \rightarrow \mathrm{Mg_2X},$$

as

$$E_{form} = E(\mathrm{Mg_2X}) - 2E(\mathrm{Mg}) - E(\mathrm{X}).$$

In order to study the thermodynamic stability, the atomic chemical potentials (μ) must be considered under some specific constrains of the bulk elements[49,50]. For these particular alloys, we generalize the equation of the formation energy of $Mg_2X_{1-x}Y_x$, obtained through the reaction

$$2\mathrm{Mg} + (1-x)\mathrm{X} + x\mathrm{Y} \rightarrow \mathrm{Mg_2X_{1-x}Y_x}, \tag{1}$$

as

$$E_{Form} = E(\mathrm{Mg_2X}) - 2\mu(\mathrm{Mg}) - (1-x)\mu(\mathrm{X}) - x\mu(\mathrm{Y}). \tag{2}$$

The chemical potentials of Eq. (2) in the Mg-rich region are given by

$$\begin{aligned} \mu(\mathrm{Mg}) &= E(\mathrm{Mg}), \\ \mu(\mathrm{X}) &= E(\mathrm{Mg_2X}) - 2E(\mathrm{Mg}), \\ \text{and } \mu(\mathrm{Y}) &= E(\mathrm{Mg_2Y}) - 2E(\mathrm{Mg}). \end{aligned} \tag{3}$$

Therefore, the relative formation energy given by Eqs. (2) and (3) vanishes at the end compounds, $x = 0$ and $x = 1$. We present our calculated relative formation energies for all quasi-binary $Mg_2X_{1-x}Y_x$ alloys in Fig. 1, in the compositional space x, using a resolution of $\Delta x = 0.1$. We also compare our results with other theoretical findings previously reported. We note that the currently available data correspond to the $Mg_2Si_{1-x}Ge_x$ systems[32], and $Mg_2Si_{1-x}Sn_x$[32,35]. No results have been reported so far about theoretical or experimental formation energies in $Mg_2Ge_{1-x}Sn_x$. We observe that the relative formation energy of the $Mg_2Si_{1-x}Ge_x$ systems are nearly vanishing, and this result corroborates the observed solubility and thermodynamical stability at all compositions[15]. In contrast, in $Mg_2Si_{1-x}Sn_x$ and $Mg_2Ge_{1-x}Sn_x$, the positive formation energies indicate a lower stability and therefore a possible miscibility gap[1,21,24,51–54]. Our calculations reveal that the formation energies of $Mg_2Ge_{1-x}Sn_x$ lie below that of $Mg_2Si_{1-x}Sn_x$ and that both fit a cubic polynomial with maximal value at a content of $x \approx 0.43$ of Sn. We attribute this non-symmetric curve to the non-linear character of volumetric dependence of the alloys with composition[38], in contrast to the symmetric behavior observed in other calculations presented in Fig. 1

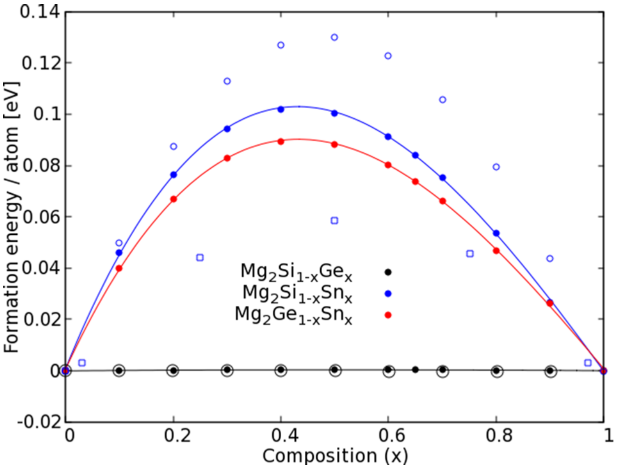

Figure 1. Relative formation energy per atom defined by Eq. (2), of the $Mg_2X_{1-x}Y_x$ alloys. Our calculations are presented using the solid dots as labeled, and the connecting lines correspond to a cubic polynomial fit. The empty circles[32] and squares[24] are calculations taken from literature, shown in black for $Mg_2Si_{1-x}Ge_x$ and in blue for $Mg_2Si_{1-x}Sn_x$.

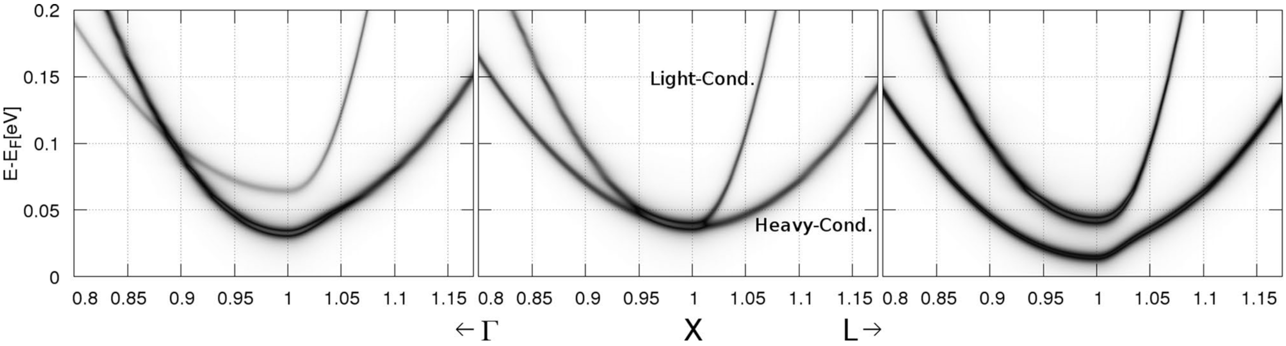

Figure 2. Low-lying light- and heavy-conduction bands of $Mg_2Ge_{1-x}Sn_x$ at compositions near the crossing, $x = 0.65$ (left), $x = 0.7$ (center), and $x = 0.75$ (right), in the vicinity of the X-point [100] along $X - \Gamma$ and $X - L$, with k in units of $2\pi/a$ (dark gray corresponds to high BSF in a.u.).

that assumed that Vegard's law holds. We also note that there is no direct experimental data to compare the formation energy since experiments are performed at room temperature, or higher, and it is also frequent to use temperature dependent phase diagrams[24], or different approaches to investigate materials stability[54–56]. Solubility of these alloys is still under debate since, despite the existence of the miscibility gap, experiments have been reported for compositions between this gap[29], and other experiments show instabilities based on variations of the measurements as the temperature increases and decreases[30]. Therefore we can interpret that the experimental conditions influence their stability and can lead to stable phases, as it is the case of e.g. the mechanical alloying technique[24,29,46,57].

Effective mass parameters of the conduction bands. Within the CPA, using the total energy calculations presented in the Methods section and adequate structural parameters[38], we compute the Bloch spectral function (BSF) to map the electronic bands and to extract information about the electronic states in the $Mg_2X_{1-x}Y_x$ alloys[58,59]. The CPA mimics the alloying effects on the electronic states a physical broadening, since it considers a uniform and randomly distributed bulk alloy. This broadening is even more pronounced for those bands that displace in energy as the composition changes, and thus fitting a rigid band with single k-value becomes a numerical challenge. We fit the bands using a Lorentzian profile and we test parabolicity to hold in an energy window up to $\approx$ 0.1 eV ($k \approx 0.03\ 2\pi/a$, a is the lattice constant[38]), as illustrated in Fig. 2[60]. Using these fitted k-values, we obtain the parabolic band effective mass at the X [100] point, along the $\vec{k}$-direction, using the formula

$$E(k) = E_0 + \frac{\hbar^2}{2m^*}(k - \mathrm{X})^2, \tag{4}$$

where $\hbar = h/2\pi$ is the reduced Plank's constant, m^* is the effective mass along $\vec{k}$ (k is the norm of $\vec{k}$), and E_0 corresponds to the indirect band gap. Hence, we extract the band effective mass (m^*) from the inverse of the

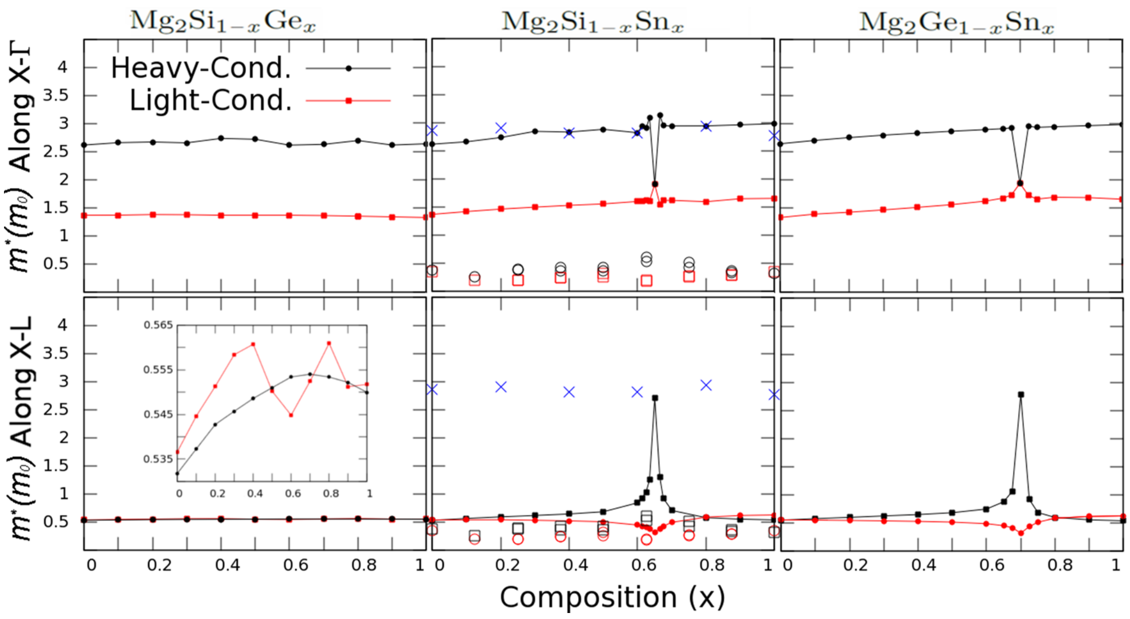

Figure 3. Parabolic band effective mass calculations corresponding to $Mg_2Si_{1-x}Ge_x$ (left), $Mg_2Si_{1-x}Sn_x$ (center), and $Mg_2Ge_{1-x}Sn_x$ (right), along the $X-\Gamma$ (top) and $X-L$ (bottom) directions, as function of the composition x. The available experimental data for $Mg_2Si_{1-x}Sn_x$ is presented using the blue X symbols[30], while theoretical data is presented using the black and red empty symbols to represent the HC and LC effective masses, respectively[31,65].

curvature of the parabola. To measure anisotropic effects on transport, the experimental samples must be perfectly mono-crystalline and oriented along different crystallographic directions, as ruled by Eq. (4). Experiments are rather performed in randomly oriented samples and therefore the measurements correspond to an averaged effective mass over the reciprocal k-space. In order to avoid a very expensive integration, we compute the effective mass for each conduction band along different directions using Eq. (4). We have already successfully computed the effective masses of the conduction and valence bands located at the zone center—the Γ point—of the BZ, using this generalized effective mass definition[38]. We have also found, that the (Lorentzian) broadening of the bands is on the order of $\sim$ 1% measured relative to the parabolic domain, and is more pronounced in the heavy conduction band as we present in Fig. 2.

In Fig. 2 we present the conduction bands of $Mg_2Ge_{1-x}Sn_x$ near the crossing point, that we determine to be at $x = 0.7$. The bands of $Mg_2Si_{1-x}Sn_x$ present a similar behavior near the crossing point that we determine to take place at $x = 0.65$. This crossing is therefore controlled by the composition x that also controls the size of the unit cell[38]. This implies, that at room temperatures the thermal expansion must be considered and the crossing points are expected to take place at a lower composition, i.e., near $x = 0.6$ for $Mg_2Si_{1-x}Sn_x$[61–64]. We label the bands in Fig. 2 as *light*-conduction (LC) and *heavy*-conduction (HC) bands according to their effective mass. We note that both bands present a crossing along $\Gamma - X$ for compositions below $x = 0.7$. Along $X - L$ we observe no crossing. This crossing moves down in energy by increasing the composition x of Sn, then the electron pockets merge at $x = 0.7$[32], and then, for larger compositions, the crossing disappears in both directions. We also note, that the curvature and the degeneracy of the bands are strongly dependent on the direction in the BZ. Along $X - \Gamma$, both bands show a wider degeneracy range, up to nearly $\sim 0.05(2\pi/a)$, compared to a range of nearly $\sim 0.01(2\pi/a)$ along $X - L$. This means, that the effective mass along $X - \Gamma$ must coincide for both conduction bands, while these bands are distinguishable along $X - L$ as their effective masses are. Additionally, the resulting masses must be different along both directions, especially for the LC band that is heavier along $X - \Gamma$.

We present the computed effective masses (m^*), measured in units of the electron's rest mass (m_0), as function of the composition for the $Mg_2X_{1-x}Y_x$ thermoelectric alloys in Fig. 3 along the directions given by Fig. 2. In the left column of Fig. 3 we show the $Mg_2Si_{1-x}Ge_x$ system, in which the heavy- and light-conduction bands increase slow and constantly with the composition, and its value strongly depends on the direction. Along $X - \Gamma$, m^*_{HC} and m^*_{LC} keep a constant ratio of about 1.7, while along $X - L$ both bands are nearly similar, $m^*_{LC} \approx m^*_{HC} \approx 0.5m_0$. As shown in the inset of Fig. 3, and pointed out before, alloying effects are more remarkable in the HC band thus making it difficult to uniquely determine the effective mass.

In Fig. 3 we also present our computed effective masses for $Mg_2Si_{1-x}Sn_x$ (center) and $Mg_2Ge_{1-x}Sn_x$ (right) systems along $\Gamma - X$ (up) and $X - L$ (down). For $Mg_2Si_{1-x}Sn_x$, we include available experimental and theoretical data[30,31,65]. We point out, that the measured (DOS) effective masses correspond to $\tilde{m}^* = (N_v)^{2/3} m^*$, where N_v is the degeneracy of the bands and m^* corresponds to either a single pocket effective mass[31], or an average of the bands[30]. The experimental data shown in Fig. 3 correspond to an average over the effective masses and does not manifest a degeneracy peak ($N_v = 2$) at the crossing point. However, the experimental trend is very well described by our computed effective masses along $X - \Gamma$ considering that $N_v = 1$, for x away from the crossing point. At this point, both bands are degenerate and have the same effective mass $m^* \approx 1.85m_0$, that multiplied by the degeneracy $N_v^{2/3} \approx 1.59$, coincides with the experimental value presented there.

Recently, using the DFT-supercell approach, and unfolding-back the BZ, band's convergence in $Mg_2Si_{1-x}Sn_x$ was systematically studied as function of the unit cell volume—using Vegard's law—to clarify the orbital composition of the bands and energy gaps[66]. On the other hand, the theoretical effective masses taken from literature and shown in Fig. 3 predict the crossing at compositions between $x = 0.6-0.7$, nearly $x = 0.625$, for $Mg_2Si_{1-x}Sn_x$, due to a limited resolution of the chemical-compositional space offered by the DFT-supercell approach[31,65]. These masses are not allowed to change for different orientations in the BZ and both data sources show similar numerical values. The trends of these masses as function of the composition are very well described by our calculations along $X - L$, especially the decrease reported in the LC mass by nearly a 40%, as we similarly report. Along $X - L$, the bands are distinguishable, and the computed masses from literature show an enhancement near to 45% thus improving the absolute value of the PF by nearly 60–80%. In these materials, the optimal thermoelectric performance is found at $T \approx 750$ K, with an approximate dependency on the effective mass is given by $PF \sim (m^*)^{3/2}$. We concentrate at the crossing points and we include extra calculations to have a higher resolution close to this point. Our HC band is predicted to increase by a factor of $\sim$ 5 and, without degeneracy, this value coincides with the experimentally measured mass. In $Mg_2Si_{1-x}Sn_x$, the Seebeck coefficient has been computed and enhances by nearly 50%[31]. Our computations represent the building block for macroscopic transport simulations using, e.g., the semi-classical multi-band approach to transport—the Boltzmann transport equation—within the relaxation time approximation. Transport simulations require extra approximations and, e.g., the consideration of the electronic mobility to account for bipolar effects[60,67]. We extrapolate this study to predict the transport parameters for $Mg_2Ge_{1-x}Sn_x$ that show a similar behavior compared to $Mg_2Si_{1-x}Sn_x$ and have not been yet published.

Discussion

We have used the DFT-based Green's functions KKR formalism in the full relativistic case, within the CPA for describing the electronic properties of the $Mg_2X_{1-x}Sn_x$ alloys. After carefully study of the structural details, within the LDA, we compute the formation energy that sheds lights on structural stability, specially about the existing miscibility gap between Mg_2X (X=Si,Ge) and Mg_2Sn. We conclude that, in spite of the existence of a experimentally reported miscibility gap in the $Mg_2X_{1-x}Sn_x$ systems, many experiments have reported their stability during the measurements but many others have shown inconsistent results. Therefore, the solubility of these alloys depend on the experimental conditions that overcome the excess of formation energy. We predict the exact composition at which the conduction bands merge in $Mg_2X_{1-x}Sn_x$ and we interpret other experimental and theoretical results by fitting a detailed band structures near the crossing points. Our calculations have shown a very good agreement with other results and allow us to predict intermediate data not published so far.

Methods

The computational details of the present work are based on a previous report[38]. We use the Green's functions based Korringa–Kohn–Rostocker (KKR) formalism, in full-relativistic description[68], and within the local density approximation (LDA) for treating the exchange-correlation potential[69]. For the electronic properties of a homogeneous alloy phase, we map the complex band structure using a Bloch spectral density function (BSF) defined within the coherent potential approximation (CPA)[58]. The CPA is a very efficient approach to the alloy problem since it strongly reduces computational costs without folding the BZ. Since CPA considers uniformly random bulk alloys to construct an efficient complex-potential, CPA describes the broadening on the bands due to chemical disorder. This task would be in principle very difficult to reach using a supercell-DFT approach since it would require the computation over a very large—in principle infinite—number of configurations. Moreover, we are allowed to define a randomly fine chemical space of compositions near the crossing points, which is also a very hard task for the supercell approach. We assume the anti-fluorite ($Fm\bar{3}m$) crystallization of the Mg_2X compounds and their intermediate alloys, with lowest conduction bands at the X-point. The X = Si, Ge, Sn atoms form a diamond cubic structure while the Mg atoms have a hexagonal close-packed structure[1]. Our results have shown a very good agreement with available experimental data and represent a good source of—to the date—unavailable intermediate data in these alloy systems. Therefore, we retain the computational scheme to extract the relative formation energy from the total energy calculations, within the atomic sphere approximation (ASA).

Received: 12 March 2020; Accepted: 27 August 2020
Published online: 01 October 2020

References

1. Rowe, D. *CRC Handbook of Thermoelectrics* (CRC-Press, Boca Raton, 1995). https://doi.org/10.1201/9781420038903 .
2. Bahk, J.-H., Bian, Z. & Shakouri, A. Electron transport modeling and energy filtering for efficient thermoelectric $Mg_2Si_{1-x}Sn_x$ solid solutions. *Phys. Rev. B* **89**, 075204. https://doi.org/10.1103/PhysRevB.89.075204 (2014).
3. Nikitin, E. N. & Bazanov, V. G. The thermoelectric properties of solid solution, $Mg_2Si - Mg_2Sn$. *Sov. Phys. Sol. State* **3**, 2648 (1961).
4. Fedorov, M. I., Zaitsev, V. K. & Isachenko, G. N. In *Solid Compounds of Transition Elements, Solid State Phenomena* Vol. 170, 286–292 (Trans Tech Publications, 2011). https://doi.org/10.4028/www.scientific.net/SSP.170.286.
5. Winkler, U. Electric properties of the intermetallic compounds Mg_2Si, Mg_2Ge, Mg_2Sn, and Mg_2Pb. *Helv. Phys. Acta* **28**, 633 (1955).
6. Morris, R. G., Redin, R. D. & Danielson, G. C. Semiconducting properties of Mg_2Si single crystals. *Phys. Rev.* **109**, 1909. https://doi.org/10.1103/PhysRev.109.1909 (1958).
7. Redin, R. D., Morris, R. G. & Danielson, G. C. Semiconducting properties of Mg_2Ge single crystals. *Phys. Rev.* **109**, 1916. https://doi.org/10.1103/PhysRev.109.1916 (1958).

8. Mead, C. A. Photothresholds in Mg$_2$Ge. *J. Appl. Phys.* **35**, 2460. https://doi.org/10.1063/1.1702881 (1964).
9. Blunt, R. F., Frederikse, H. P. R. & Hosler, W. R. Electrical and optical properties of intermetallic compounds. IV. Magnesium stannide. *Phys. Rev.* **100**, 663. https://doi.org/10.1103/PhysRev.100.663 (1955).
10. Vazquez, F., Forman, R. A. & Cardona, M. Electroreflectance measurements on Mg $_2$Si, Mg $_2$Ge, and Mg $_2$Sn. *Phys. Rev.* **176**, 905. https://doi.org/10.1103/PhysRev.176.905 (1968).
11. Heller, M. & Danielson, G. Seebeck effect in Mg $_2$ Si single crystals. *J. Phys. Chem. Sol.* **23**, 265. https://doi.org/10.1016/0022-3697(62)90519-X (1962).
12. Ober, J. A. *Mineral Commodity Summaries* (U.S. Geological Survey, 2018). https://www.usgs.gov/centers/nmic/mineral-commodity-summaries
13. Hsu, D. D. Chemicool periodic table (2018). http://www.chemicool.com
14. Zaitsev, V. K. *et al.* Highly effective Mg $_2$ Si $_{1-x}$ Sn $_x$ thermoelectrics. *Phys. Rev. B* **74**, 045207. https://doi.org/10.1103/PhysRevB.74.045207 (2006).
15. LaBotz, R. J., Mason, D. R. & O'kane, D. F. The thermoelectric properties of mixed crystals of Mg $_2$ Ge$_x$ Si$_{1-x}$. *J. Electrochem. Soc.* **110**, 127. https://doi.org/10.1149/1.2425689 (1963).
16. Stella, A., Brothers, A. D., Hopkins, R. H. & Lynch, D. W. Pressure coefficient of the band gap in Mg$_2$Si, Mg$_2$Ge, and Mg$_2$Sn. *Phys. Status Solidi (B)* **23**, 697 (1967).
17. Lott, L. A. & Lynch, D. W. Infrared absorption in Mg $_2$Ge. *Phys. Rev.* **141**, 681. https://doi.org/10.1103/PhysRev.141.681 (1966).
18. Lipson, H. G. & Kahan, A. Infrared absorption of magnesium stannide. *Phys. Rev.* **133**, A800. https://doi.org/10.1103/PhysRev.133.A800 (1964).
19. Scouler, W. J. Optical properties of Mg_2Si, Mg_2Ge, and Mg_2Sn from 0.6 to 11.0 eV at 77 K. *Phys. Rev.* **178**, 1353. https://doi.org/10.1103/PhysRev.178.1353 (1969).
20. Koenig, P., Lynch, D. & Danielson, G. Infrared absorption in magnesium silicide and magnesium germanide. *J. Phys. Chem. Solids* **20**, 122. https://doi.org/10.1016/0022-3697(61)90142-1 (1961).
21. Bhattacharya, S. & Madsen, G. K. H. High-throughput exploration of alloying as design strategy for thermoelectrics. *Phys. Rev. B* **92**, 085205. https://doi.org/10.1103/PhysRevB.92.085205 (2015).
22. Dasgupta, T., Stiewe, C., de Boor, J. & Müller, E. Influence of power factor enhancement on the thermoelectric figure of merit in Mg$_2$Si$_0$.4Sn$_0$.6 based materials. *Phys. Status Solidi (A)* **211**, 1250. https://doi.org/10.1002/pssa.201300196 (2014).
23. Isoda, Y., Nagai, T., Fujiu, H., Imai, Y., & Shinohara, Y. In *2006 25th International Conference on Thermoelectrics* 406–410 (2006). https://doi.org/10.1109/ICT.2006.331283
24. Viennois, R., Jund, P., Colinet, C. & Tédenac, J.-C. Defect and phase stability of solid solutions of Mg2X with an antifluorite structure: an ab initio study. *J. Solid State Chem.* **193**, 133. https://doi.org/10.1016/j.jssc.2012.04.048 (2012) (**solid State Chemistry and Materials Science of Thermoelectric Materials**).
25. Noda, Y., Kon, H., Furukawa, Y., Nishida, I. A. & Masumoto, K. Temperature dependence of thermoelectric properties of Mg $_2$ Si $_{0.6}$ Ge $_{0.4}$. *Mater. Trans. JIM* **33**, 851 (1992).
26. Akasaka, M., Iida, T., Nishio, K. & Takanashi, Y. Composition dependent thermoelectric properties of sintered Mg $_2$ Si $_{1-x}$ Ge $_x$ (x=0 to 1) initiated from a melt-grown polycrystalline source. *Thin Solid Films* **515**, 8237. https://doi.org/10.1016/j.tsf.2007.02.053 (2007) (**aPAC-SILICIDE 2006**).
27. Ratai, E., Augustine, M. P. & Kauzlarich, S. M. Synthesis and characterization of the Mg $_2$ Si $_x$ Ge $_{1-x}$ solid solution. *J. Phys. Chem. B* **107**, 12573. https://doi.org/10.1021/jp030252x (2003).
28. Zaitsev, V. K., Isachenko, G. N. & Burkov, A. T. In *Thermoelectrics for Power Generation—A Look at Trends in the Technology*, Chap. 11 (eds Skipidarov, S. & Nikitin, M.) (InTech, Rijeka, 2016). https://doi.org/10.5772/65864.
29. Song, R., Aizawa, T. & Sun, J. Synthesis of Mg $_2$ Si $_{1-x}$ Sn $_x$ solid solutions as thermoelectric materials by bulk mechanical alloying and hot pressing. *Mater. Sci. Eng. B* **136**, 111. https://doi.org/10.1016/j.mseb.2006.09.011 (2007).
30. Mao, J. *et al.* Thermoelectric properties of materials near the band crossing line in Mg $_2$ Sn $-$ Mg $_2$ Ge $-$ Mg $_2$ Si system. *Acta Mater.* **103**, 633. https://doi.org/10.1016/j.actamat.2015.11.006 (2016).
31. Liu, W. *et al.* Convergence of conduction bands as a means of enhancing thermoelectric performance of *n*-type Mg $_2$ Si $_{1-x}$ Sn $_x$ solid solutions. *Phys. Rev. Lett.* **108**, 166601. https://doi.org/10.1103/PhysRevLett.108.166601 (2012) (**See supplemental material**).
32. Zwolenski, P., Tobola, J. & Kaprzyk, S. A theoretical search for efficient dopants in Mg $_2$ X (X= Si, Ge, Sn) thermoelectric materials. *J. Electron. Mater.* **40**, 889. https://doi.org/10.1007/s11664-011-1624-y (2011).
33. Pei, Y., Wang, H. & Snyder, G. J. Band engineering of thermoelectric materials. *Adv. Mater.* **24**, 6125. https://doi.org/10.1002/adma.201202919 (2012).
34. Zhang, L. *et al.* Suppressing the bipolar contribution to the thermoelectric properties of Mg$_2$Si$_{0.4}$Sn$_{0.6}$ by Ge substitution. *J. Appl. Phys.* **117**, 155103. https://doi.org/10.1063/1.4918311 (2015).
35. Tobola, J., Kaprzyk, S. & Scherrer, H. Mg-vacancy-induced semiconducting properties in Mg2Si1-xSbx from electronic structure calculations. *J. Electron. Mater.* **39**, 2064. https://doi.org/10.1007/s11664-009-1000-3 (2010).
36. Kim, S., Wiendlocha, B., Jin, H., Tobola, J. & Heremans, J. P. Electronic structure and thermoelectric properties of p-type Ag-doped Mg2Sn and Mg2Sn1-xSix (x = 0.05, 0.1). *J. Appl. Phys.* **116**, 153706. https://doi.org/10.1063/1.4898013 (2014).
37. Vegard, L. Die Konstitution der Mischkristalle und die Raumfüllung der Atome. *Z. Phys.* **5**, 17. https://doi.org/10.1007/BF01349680 (1921).
38. Guerra, J. M., Mahr, C., Giar, M., Czerner, M. & Heiliger, C. Ab initio calculations of electronic band structure and effective-mass parameters of thermoelectric Mg $_2X_{1-x}Y_x(X, Y =$ Si, Ge, or Sn) pseudobinary alloys. *Phys. Rev. Mater.* **2**, 104605. https://doi.org/10.1103/PhysRevMaterials.2.104605 (2018).
39. Pulikkotil, J. J., Alshareef, H. N. & Schwingenschlögl, U. Variation of equation of state parameters in the Mg $_2$(Si $_{1-x}$ Sn $_x$) alloys. *J. Phys. Condens. Matter* **22**, 352204. https://doi.org/10.1088/0953-8984/22/35/352204 (2010).
40. Manzoor, A., Pandey, S., Chakraborty, D., Phillpot, S. R. & Aidhy, D. S. Entropy contributions to phase stability in binary random solid solutions. *NPJ Comput. Mater.* **4**, 47. https://doi.org/10.1038/s41524-018-0102-y (2018).
41. Kirklin, S. *et al.* The Open Quantum Materials Database (OQMD): assessing the accuracy of DFT formation energies. *NPJ Comput. Mater.* **1**, 15010. https://doi.org/10.1038/npjcompumats.2015.10 (2015).
42. Ye, W., Chen, C., Wang, Z., Chu, I.-H. & Ong, S. P. Deep neural networks for accurate predictions of crystal stability. *Nat. Commun.* **9**, 3800. https://doi.org/10.1038/s41467-018-06322-x (2018).
43. Ma, J. *et al.* Computational investigation of inverse Heusler compounds for spintronics applications. *Phys. Rev. B* **98**, 094410. https://doi.org/10.1103/PhysRevB.98.094410 (2018).
44. Opahle, I., Madsen, G. K. H. & Drautz, R. High throughput density functional investigations of the stability, electronic structure and thermoelectric properties of binary silicides. *Phys. Chem. Chem. Phys.* **14**, 16197. https://doi.org/10.1039/C2CP41826F (2012).
45. ichi Tani, J. & Kido, H. Thermoelectric properties of Sb-doped Mg2Si semiconductors. *Intermetallics* **15**, 1202. https://doi.org/10.1016/j.intermet.2007.02.009 (2007).
46. Viennois, R., Colinet, C., Jund, P. & Tédenac, J.-C. Phase stability of ternary antifluorite type compounds in the quasi-binary systems Mg $_2$ X $-$ Mg $_2$ Y (X, Y = Si, Ge, Sn) via ab-initio calculations. *Intermetallics* **31**, 145. https://doi.org/10.1016/j.intermet.2012.06.016 (2012).
47. Hirayama, N. *et al.* Theoretical analysis of structure and formation energy of impurity-doped Mg$_2$Si: comparison of first-principles codes for material properties. *Jpn. J. Appl. Phys.* **54**, 07JC05. https://doi.org/10.7567/JJAP.54.07JC05 (2015).

48. Jund, P. *et al.* Lattice stability and formation energies of intrinsic defects in Mg_2Si and Mg_2Ge via first principles simulations. *J. Phys. Condens. Matter* **25**, 035403. https://doi.org/10.1088/0953-8984/25/3/035403 (2012).
49. Qian, G.-X., Martin, R. M. & Chadi, D. J. First-principles study of the atomic reconstructions and energies of Ga- and As-stabilized GaAs(100) surfaces. *Phys. Rev. B* **38**, 7649. https://doi.org/10.1103/PhysRevB.38.7649 (1988).
50. Zhang, S. B. & Northrup, J. E. Chemical potential dependence of defect formation energies in GaAs: application to Ga self-diffusion. *Phys. Rev. Lett.* **67**, 2339. https://doi.org/10.1103/PhysRevLett.67.2339 (1991).
51. Kozlov, A., Gröbner, J. & Schmid-Fetzer, R. Phase formation in Mg–Sn–Si and Mg—Sn—Si–Ca alloys. *J. Alloys Compd.* **509**, 3326. https://doi.org/10.1016/j.jallcom.2010.12.052 (2011).
52. Jung, I.-H. & Kim, J. Thermodynamic modeling of the Mg–Ge–Si, Mg–Ge–Sn, Mg–Pb–Si and Mg–Pb–Sn systems. *J. Alloys Compd.* **494**, 137. https://doi.org/10.1016/j.jallcom.2010.01.045 (2010).
53. Jung, I.-H., Kang, D.-H., Park, W.-J., Kim, N. J. & Ahn, S. Thermodynamic modeling of the Mg–Si–Sn system. *Calphad* **31**, 192. https://doi.org/10.1016/j.calphad.2006.12.003 (2007).
54. Zhang, Q., Zhao, X. B., Zhu, T. J. & Tu, J. P. Ab-initio thermodynamic calculations of Mg2BIV (BIV = Si, Ge, Sn) solid solutions. *Phys. Status Solidi (RRL) Rapid Res. Lett.* **2**, 56. https://doi.org/10.1002/pssr.200701299 (2008).
55. Korzhavyi, P. A. *et al.* Constitutional and thermal point defects in B2 NiAl. *Phys. Rev. B* **61**, 6003. https://doi.org/10.1103/PhysRevB.61.6003 (2000).
56. Krachler, R., Semenova, O. & Ipser, H. A Statistical-thermodynamic model for intermetallic phases with L12-structure and its application to the compound Ni3Al. *Phys. Status Solidi (B)* **216**, 943. https://doi.org/10.1002/(SICI)1521-3951(199912)216:2<943::AID-PSSB943>3.0.CO;2-6 (1999).
57. Yi, S.-I. *et al.* Strain-induced suppression of the miscibility gap in nanostructured $Mg_2Si - Mg_2Sn$ solid solutions. *J. Mater. Chem. A* **6**, 17559. https://doi.org/10.1039/C8TA05798B (2018).
58. Franz, C., Czerner, M. & Heiliger, C. Influence of the magnetic material on tunneling magnetoresistance and spin-transfer torque in tunnel junctions: ab initio studies. *Phys. Rev. B* **88**, 094421. https://doi.org/10.1103/PhysRevB.88.094421 (2013).
59. Soven, P. Coherent-potential model of substitutional disordered alloys. *Phys. Rev.* **156**, 809. https://doi.org/10.1103/PhysRev.156.809 (1967).
60. Liu, W. *et al.* Advanced thermoelectrics governed by a single parabolic band: $Mg_2Si_{0.3}Sn_{0.7}$, a canonical example. *Phys. Chem. Chem. Phys.* **16**, 6893. https://doi.org/10.1039/c4cp00641k (2014).
61. Du, Z. *et al.* Roles of interstitial Mg in improving thermoelectric properties of Sb-doped $Mg_2Si_{0.4}Sn_{0.6}$ solid solutions. *J. Mater. Chem.* **22**, 6838. https://doi.org/10.1039/C2JM16694A (2012).
62. Fedorov, M. I., Zaitsev, V. K., Isachenko, G. N., Eremin, I. S., Gurieva, E. A., Burkov, A. T., Konstantinov, P. P., Shabaldin, A. A. In *ICT 2005. 24th International Conference on Thermoelectrics, 2005* 110–113 (2005). https://doi.org/10.1109/ICT.2005.1519900
63. Ihou-Mouko, H., Mercier, C., Tobola, J., Pont, G. & Scherrer, H. Thermoelectric properties and electronic structure of p-type Mg_2Si and $Mg_2Si_{0.6}Ge_{0.4}$ compounds doped with Ga. *J. Alloys Compd.* **509**, 6503. https://doi.org/10.1016/j.jallcom.2011.03.081 (2011).
64. Isachenko, G. N. *et al.* Kinetic properties of p-$Mg_2Si_xSn_{1-x}$ solid solutions for $x < 0.4$. *Phys. Solid State* **51**, 1796. https://doi.org/10.1134/S1063783409090066 (2009).
65. Tan, X. J. *et al.* Multiscale calculations of thermoelectric properties of *n*-type $Mg_2Si_{1-x}Sn_x$ solid solutions. *Phys. Rev. B* **85**, 205212. https://doi.org/10.1103/PhysRevB.85.205212 (2012).
66. Tan, X. *et al.* Understanding the band engineering in Mg_2Si-based systems from Wannier–Orbital analysis. *Ann. Phys.*, 1900543. https://onlinelibrary.wiley.com/doi/pdf/10.1002/andp.201900543
67. Liu, X. *et al.* Low electron scattering potentials in high performance $Mg_2Si_{0.45}Sn_{0.55}$ based thermoelectric solid solutions with band convergence. *Adv. Energy Mater.* **3**, 1238. https://doi.org/10.1002/aenm.201300174 (2013).
68. Czerner, M., Yavorsky, B. & Mertig, I. The role of noncollinear magnetic order and magnetic anisotropy for the transport properties through nanowires. *Phys. Status Solidi (B)* **247**, 2594. https://doi.org/10.1002/pssb.201046190 (2010).
69. Gunnarsson, O. & Lundqvist, B. I. Exchange and correlation in atoms, molecules, and solids by the spin-density-functional formalism. *Phys. Rev. B* **13**, 4274. https://doi.org/10.1103/PhysRevB.13.4274 (1976).

Acknowledgements

Financial support is provided by the DFG via the GRK (Research Training Group) 2204 "Substitute Materials for sustainable Energy Technologies".

Author contributions

J.M.G. performed the calculations and wrote the manuscript, C.M. and M.G. provided valuable tools and scripts for the calculations, M.C. provided valuable guide concerning the theoretical approach and computational methods, and C.H. coordinated all the work. All authors reviewed and commented on the manuscript.

Funding

Open Access funding enabled and organized by Projekt DEAL.

Competing interests

The authors declare no competing interests.

Additional information

Correspondence and requests for materials should be addressed to J.M.G.

Reprints and permissions information is available at www.nature.com/reprints.

Publisher's note Springer Nature remains neutral with regard to jurisdictional claims in published maps and institutional affiliations.

Open Access This article is licensed under a Creative Commons Attribution 4.0 International License, which permits use, sharing, adaptation, distribution and reproduction in any medium or format, as long as you give appropriate credit to the original author(s) and the source, provide a link to the Creative Commons licence, and indicate if changes were made. The images or other third party material in this article are included in the article's Creative Commons licence, unless indicated otherwise in a credit line to the material. If material is not included in the article's Creative Commons licence and your intended use is not permitted by statutory regulation or exceeds the permitted use, you will need to obtain permission directly from the copyright holder. To view a copy of this licence, visit http://creativecommons.org/licenses/by/4.0/.

© The Author(s) 2020